Original Article

Quantification of infrapatellar fat pad fibrosis using magnetic resonance imaging-derived proton density fat fraction: a pathology-controlled study

Beibei Zhou[1,2,3#], Jinling Wu[1,2#], Tianyun Zhao[4,5], Qingling Yu[1,2], Kexin Jiang[1,2], Xinru Zhang[1,2], Qingzhu Wei[6], Rongkai Zhang[7], Hang Fang[7], Hongbo Zhang[3], Yanjun Chen[1,2], Xiaodong Zhang[1,2], Chuan Huang[4,5]

[1]The Third School of Clinical Medicine, Southern Medical University, Guangzhou, China; [2]Department of Radiology, The Third Affiliated Hospital, Southern Medical University, Guangzhou, China; [3]Department of Radiology, The Seventh Affiliated Hospital, Sun Yat-sen University, Shenzhen, China; [4]Department of Biomedical Engineering, Stony Brook University, Stony Brook, NY, USA; [5]Department of Radiology and Imaging Sciences, Emory University, Atlanta, GA, USA; [6]Department of Pathology, The Third Affiliated Hospital, Southern Medical University, Guangzhou, China; [7]Department of Joint Surgery, Center for Orthopedic Surgery, The Third Affiliated Hospital, Southern Medical University, Guangzhou, China

Contributions: (I) Conception and design: Xiaodong Zhang, C Huang, Y Chen; (II) Administrative support: Xiaodong Zhang, Y Chen; (III) Provision of study materials or patients: Q Wei, R Zhang, H Fang; (IV) Collection and assembly of data: B Zhou, J Wu, Q Yu, K Jiang, Xinru Zhang; (V) Data analysis and interpretation: B Zhou, J Wu, T Zhao, H Zhang; (VI) Manuscript writing: All authors; (VII) Final approval of manuscript: All authors.

[#]These authors contributed equally to this work.

Correspondence to: Yanjun Chen, MD, PhD; Xiaodong Zhang, MD, PhD. Department of Radiology, The Third Affiliated Hospital, Southern Medical University, Zhongshan Avenue West, Tianhe District, Guangzhou 510515, China; The Third School of Clinical Medicine, Southern Medical University, Guangzhou, China. Email: justmedic@163.com; ddautumn@126.com.

Background: Knee osteoarthritis (KOA) is a degenerative joint disease leading to disability in the elderly. Fibrosis of the infrapatellar fat pad (IPFP) impacts knee joint function and disease progression. Accurate assessment of IPFP fibrosis aids early intervention and treatment. The aim of this study was to evaluate the diagnostic efficacy of proton density fat fraction (PDFF) and T2* measurements using mDixon-Quant technology in assessing IPFP fibrosis in KOA.

Methods: A total of 47 patients were included in this study (23 patients without fibrosis, 17 with mild fibrosis, and 7 with severe fibrosis). Knee magnetic resonance (MR) scans were performed on a 3.0 T MR system. MR sequences included 3.0 T, sagittal T2-weighted images, proton density-weighted spectral adiabatic inversion recovery (PDW-SPAIR), and three-dimensional (3D) six-echo gradient recalled echo sequence (mDixon-Quant). Two radiologists performed PDFF, T2* measurements, and the hypointense signal grade of the IPFP. Measurements were compared among the three subgroups, and correlations of the three parameters with pathology-derived IPFP fibrosis degree and diagnostic efficacy were evaluated. Intraclass correlation coefficient (ICC), one-way analysis of variance (ANOVA), and Spearman correlation analysis were used. The diagnostic performance was assessed using the area under the receiver operating characteristic (ROC) curve (AUC) and linear regression with leave-one-out cross validation. Statistical significance was set at $P<0.05$.

Results: MR measurements demonstrated good inter-observer reproducibility (ICC for PDFF =0.901, ICC for T2* =0.902). The PDFF and T2* values in the normal and mild fibrosis groups were higher than those in the severe fibrosis group. PDFF and T2* measurements were strongly correlated with IPFP fibrosis (ρ=–0.7083, –0.6028, respectively). PDFF and T2* showed good diagnostic performance for IPFP fibrosis (AUC =0.9529, 0.8098, respectively). Adjusted R^2 indicated similar results (PDFF 0.6682, T2* 0.538,

hypointense 0.1437). Using PDFF and T2* together showed good diagnostic performance for IPFP fibrosis (AUC =0.9601) and had the best R^2 of 0.6995.

Conclusions: PDFF and T2* measurements based on mDixon technology provide a non-invasive and quantitative assessment of IPFP fibrosis, especially PDFF.

Keywords: Knee osteoarthritis (KOA); infrapatellar fat pad (IPFP); fibrosis; magnetic resonance imaging (MRI); mDixon-Quant

Submitted Sep 22, 2024. Accepted for publication Jan 23, 2025. Published online Mar 18, 2025.
doi: 10.21037/qims-24-2021
View this article at: https://dx.doi.org/10.21037/qims-24-2021

Introduction

Knee osteoarthritis (KOA) is a common degenerative joint disease that involves pathological changes throughout the joint, including the cartilage, synovium, meniscus, infrapatellar fat pad (IPFP), subchondral bone, and other structures (1). KOA mainly affects the elderly population and is a major cause of disability in severe cases (2).

The IPFP, located beneath the patella, has recently garnered attention as a critical factor in KOA pathology (3). The IPFP is intracapsular yet extrasynovial; it has direct and constant contact with synovium, which produces synovial fluid for smooth joint movement. Increasingly, the IPFP and synovium are viewed as a single anatomo-functional unit rather than separate structures, acknowledging their interdependent roles in joint homeostasis and disease progression (4).

Age-related changes are known to significantly affect IPFP structure and function. Studies have reported a decline in collagen III and elastic fibers with age, whereas adipocyte area increases, suggesting age-related IPFP remodeling (5). Among the various pathological changes, IPFP fibrosis plays a key role in KOA progression. For fibrosis, inflammatory changes within the IPFP are often considered an initial pathological step, with cytokine release and immune cell infiltration contributing to tissue remodeling. However, a study showed that pro-fibrotic IPFP remodeling without M1-macrophage polarization preceded KOA in diet-induced obese mice (6). Chronic inflammation may drive fibrotic changes, characterized by excessive extracellular matrix deposition and altered tissue architecture (7).

Functionally, IPFP fibrosis not only reduces elasticity, which affects the biomechanical function of the knee joint (8), but also increases the pressure on the joint cartilage, accelerating the progression of KOA (9). Research has demonstrated that IPFP fibrosis plays a key role in knee pain and cartilage degeneration, and is important in the onset and progression of KOA (10-12). Therefore, early assessment of IPFP fibrosis can help to identify high-risk individuals, allowing for early intervention and potentially slowing disease progression.

Current techniques for assessing IPFP fibrosis are limited. Direct histological evaluation requires arthroscopic biopsy, which, although effective for assessing fibrosis severity, is invasive and impractical for routine clinical use. Alternatively, biomarkers related to IPFP fibrosis, such as cartilage oligomeric matrix protein, have been explored (13), but these methods have limitations in terms of sensitivity and specificity.

Magnetic resonance imaging (MRI) is a non-invasive, high-resolution imaging technique that has been widely used in the diagnosis and study of KOA (14-17). MRI can clearly show the morphological and signal characteristics of the IPFP. MRI can also quantify IPFP dimensions, showing a decrease in IPFP volume and an increase in hypointense signals in end-stage osteoarthritis (OA) patients (18). Increased T2-weighted or proton density-weighted signals often reflect inflammation or edema (19). Studies have found that hypointense signals in IPFP may indicate fibrosis and other knee symptoms (10). However, despite their usefulness, these methods fail to provide quantitative assessment and can be affected by readers' judgment and experience.

Chemical shift-based water-fat separation MRI offers a significant advancement by allowing quantitative assessment of proton density fat fraction (PDFF) in different tissues (20). Studies have found that IPFP fibrosis can lead to reduced fat content and decreased PDFF in adipose tissue. In addition, fibrosis and angiogenesis processes can result in reduced T2* relaxation time (21). These findings suggest the potential to use these parameters for

quantitative assessment of IPFP fibrosis. Beyond the benefit of non-invasive assessment, this imaging technique is also simple, fast, and widely available in clinical MR scanners.

The purpose of this study was to investigate the correlation between PDFF and T2* with the degree of KOA IPFP fibrosis using histology as the reference standard. Additionally, this pathology-controlled study, the first of its kind, aimed to evaluate the diagnostic efficacy of these parameters in KOA IPFP fibrosis. By leveraging histological analysis as a benchmark, this study provides robust validation of PDFF and T2* measurements. The quantitative data derived from these parameters could significantly enhance the accuracy of KOA diagnosis and the effectiveness of subsequent treatments. We present this article in accordance with the STARD reporting checklist (available at https://qims.amegroups.com/article/view/10.21037/qims-24-2021/rc).

Methods

Patients and tissue collection

The study was conducted in accordance with the Declaration of Helsinki (as revised in 2013). The study protocol was approved by the Ethics Committee of The Third Affiliated Hospital, Southern Medical University (No. 2024-lunshen-008) and informed consent was provided by all individual participants. In this study, the patients were recruited from the Department of Joint Surgery, Center for Orthopedic Surgery, The Third Affiliated Hospital, Southern Medical University. From October 2023 to April 2024, 47 participants (aged 50–83 years, average 67.1 years, 9 males and 38 females) undergoing total knee replacement (TKR) treatment took part in this study. OA was diagnosed based on clinical symptoms and radiographic findings. We used the 1986 American College of Rheumatology (ACR) criteria and/or the Kellgren-Lawrence grading (KLG) system to diagnose OA: no OA (KLG 0–1), mild OA (KLG 2), advanced OA (KLG 3–4) (22,23). Additional inclusion/exclusion criteria were as follows: (I) no known prior joint diseases (e.g., autoimmune rheumatic diseases, tumors, metastasis, or metabolic disorders); (II) no documented knee abnormalities or surgically treated knee diseases; and (III) no contraindications for MRI, such as pacemakers or cochlear implants. All patients underwent knee MR examinations the day before surgery.

All patients received TKR treatment in the orthopedics department, during which IPFP was collected, fixed in 4% paraformaldehyde, and then embedded in paraffin for histochemical studies.

Histological analysis

The IPFP was stained with Sirius Red (Phygene, Fuzhou, China, cat# PH1099) to visualize the fibrosis (24). The details about the tissue processing for histological analysis are included in Appendix 1. ImageJ software (National Institutes of Health, Bethesda, MD, USA) was used to quantify the degree of fibrosis, reported as the fraction of fibrotic area over the total cross-sectional area of the tissue (25). For quantification of fibrosis, images of Sirius Red stained sections were converted into an 8-bit image with the exclusion of the background, and the percentage area of fibrosis was calculated. Each quantification subtracted the vasculature area that was manually quantified by ImageJ software. IPFP fibrosis was also semi-quantitatively assessed using a modified IPFP score (0–≤20% normal, >20%–≤40% mild, >40%–≤60% severe, and >60% very severe) (26), with severe and very severe grouped together.

MRI

Knee MR scans were performed on a 3.0 T MR system (Ingenia; Philips Healthcare, Amsterdam, the Netherlands) using an 8-channel knee coil. All participants were examined in the head-first supine position. MR sequences included sagittal T2-weighted images, proton density-weighted spectral adiabatic inversion recovery (PDW-SPAIR), and three-dimensional (3D) six-echo gradient recalled echo (GRE) sequences (mDixon-Quant) (21,27), with a total time of approximately 4 minutes. *Table 1* shows the scanning parameters for the sequences.

MRI analysis

All MRI images were transferred to a dedicated post-processing workstation (InterlliSpace Portal; Philips) for analysis. The MRI images were independently analyzed by two radiologists (with 3 years of experience) blinded to the patient's clinical information. PDFF and T2* maps were extracted from the DIXON sequence (21). Water (W) and fat (F) images were used to calculate the PDFF using the formula (28): PDFF = F/(W + F) × 100%. T2* maps were derived from a single exponential decay model using the six-echo GRE images.

Table 1 Acquisition parameters of the sequences

Parameters	T2WI	PDW	mDixon-Quant
Acquisition plane	Sagittal	Sagittal	Sagittal
TR (ms)	1,900	2,844	8.8
TE (ms)	100	30	1.44, 2.64, 3.84, 5.04, 6.24, 7.44
FA (°)	90	90	30
Slice thickness (mm)	3.5	3.5	1.2
Matrix size (voxel)	328×174	360×360	150×150
Voxel size (mm^2)	0.55×0.88	0.5×0.5	1.2×1.2
FOV (mm^3)	180×160×92	180×180×92	180×180×96
NSA	1.3	1	1
Scan time (s)	34	120	27

T2WI, T2-weighted imaging; PDW, proton density-weighted; TR, repetition time; TE, echo time; FA, flip angle; FOV, field of view; NSA, number of signal averaging.

Regions of interest (ROIs) were manually drawn by the same radiologists in the IPFP area of the middle three slices of the PDFF images, avoiding the surrounding tissues and joint fluid. These ROIs were then copied onto T2* images for the analysis of the corresponding parameters. The quantitative results for each case were derived by averaging across the three slices.

The hypointense signal of the IPFP was evaluated using the following grade: 0= none; 1= focal fibrosis; 2= incomplete band-like fibrosis (no connection between the inferior pole of the patella and tibial plateau); 3= complete band-like fibrosis (connection between the inferior pole of the patella and tibial plateau); 4= infiltrative fibrosis; 5= diffuse and infiltrative fibrosis (occupying >75% area). The analysis was performed using T2-weighted MR images (29) by the same two radiologists.

Statistical analysis

Numerical data were reported as mean ± standard deviation (SD) for all measurements. Intraclass correlation coefficients (ICCs) with two-way random and absolute consistency were used to assess interobserver reproducibility. One-way analysis of variance (ANOVA) or Kruskal-Wallis *H* test was used to compare differences among the overall groups (normal, mild fibrosis, and severe fibrosis), followed by Tukey's or Dunn's test post hoc multiple comparisons. Spearman (ρ) was used to evaluate the correlation between MRI parameters and IPFP fibrosis.

Univariate and multivariate analyses were performed using binary logistic regression to differentiate patients into two groups: those with normal fibrosis score and those with mild or severe fibrosis score. The area under the receiver operating characteristic (ROC) curve (AUC) was calculated and ROC was compared using the DeLong test. We also conducted leave-one-out cross validation of the linear regression model, which used fibrosis percentage as the target and age, sex, and the parameters as input. Adjusted R^2 was calculated to evaluate the linear regression performance.

Statistical significance was set at $P<0.05$. All analyses were performed using MATLAB R2023a (MathWorks, Natick, MA, USA), SPSS 26.0 (IBM Corp., Armonk, NY, USA), Python (version 3.7.12; https://www.python.org/downloads/release/python-3712/) and the GraphPad Prism 9.5.0 (GraphPad Software, San Diego, CA, USA).

Results

Patient demographics and clinical characteristics

In total, 47 patients were included in this study. *Table 2* summarizes the basic clinical characteristics of all the participants. There were no significant differences in age, sex, or body mass index among the patients with different degrees of fibrosis.

Figure 1 shows the PDFF and T2* measurements and the hypointense signal grade of IPFP images corresponding

Table 2 Patient characteristics

Characteristic	Normal (n=23)	Mild fibrosis (n=17)	Severe fibrosis (n=7)	P value
Age (years)	68.3±6.7	66.5±8.9	64.6±7.4	0.4988
Sex (male/female)	5/18	3/14	1/6	0.8908
BMI (kg/m^2)	26.1±3.8	26.9±3.5	28.1±7.0	0.5885

Data are presented as number, or mean ± standard deviation (calculated using one-way ANOVA). BMI, body mass index; ANOVA, analysis of variance.

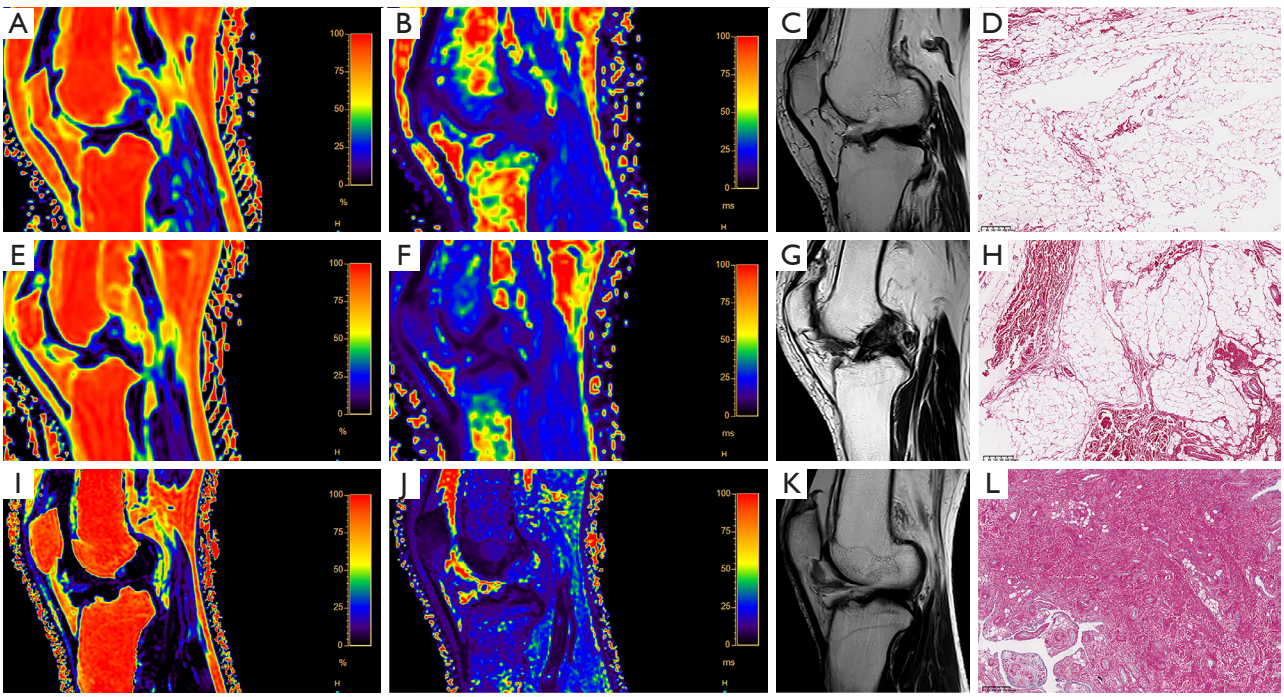

Figure 1 Images of PDFF, T2*, hypointense signal grade of IPFP, and Sirius Red staining in representative cases. (A-D) Images of PDFF, T2*, hypointense signal grade of IPFP, and Sirius Red staining in representative subjects with normal IPFP fibrosis. (E-H) Images of PDFF, T2*, hypointense signal grade of IPFP, and Sirius Red staining in representative subjects with mild IPFP fibrosis. (I-L) Images of PDFF, T2*, hypointense signal grade of IPFP, and Sirius Red staining in representative subjects with severe IPFP fibrosis. The scale bar for Sirius Red staining is 300 μm. PDFF, proton density fat fraction; IPFP, infrapatellar fat pad.

to patients with different degrees of IPFP fibrosis and the corresponding fibrosis Sirius Red staining.

Inter-observer reproducibility of MR measurements

Figure 2 shows the Bland-Altman analysis of all imaging biomarkers obtained from two radiologists' analyses of the participants. MR quantitative measurements showed excellent interobserver reproducibility. The ICC value for PDFF was 0.901 [95% confidence interval (CI): 0.827–0.944], and the ICC value for T2* was 0.902 (95% CI: 0.830–0.944), whereas the ICC value for the hypointense signal grade of the IPFP was 0.681 (95% CI: 0.483–0.811).

Differences in PDFF, T2, and hypointense signals grade of IPFP among normal, mild, and severe IPFP fibrosis groups*

The ANOVA or Kruskal-Wallis *H* test and *post hoc* analysis results are presented in *Figure 3* and *Table 3*. The group with normal IPFP fibrosis score had the highest PDFF, followed by the mild group and the severe group had the

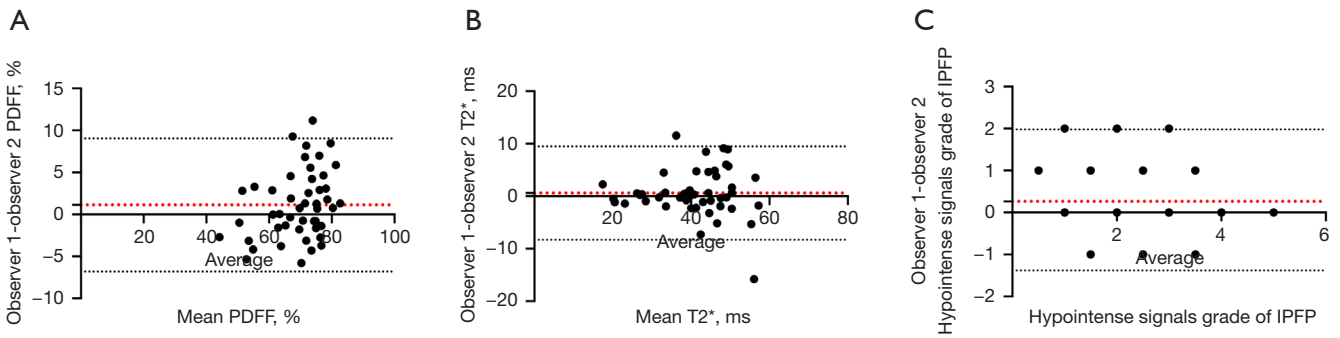

Figure 2 Bland-Altman plots for MR values. (A) Bland-Altman plot for PDFF. (B) Bland-Altman plot for T2*. (C) Bland-Altman plot for hypointense signal grade of IPFP. PDFF, proton density fat fraction; IPFP, infrapatellar fat pad; MR, magnetic resonance.

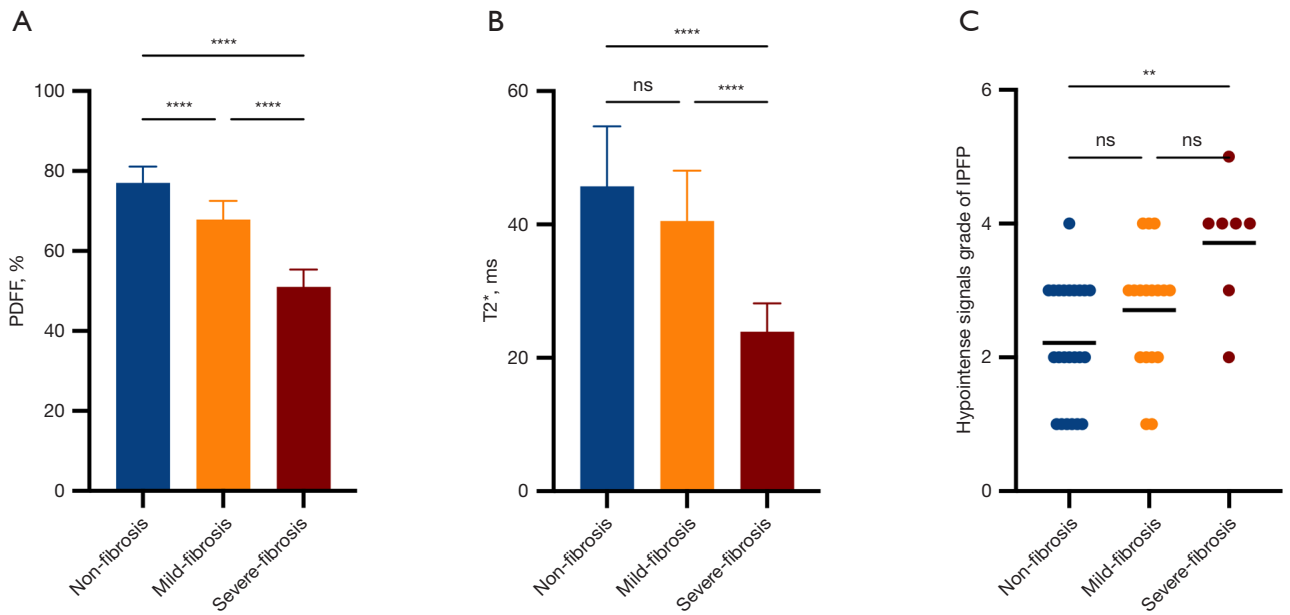

Figure 3 Bar plots and scatter plot show the differences in PDFF, T2*, and hypointense signal grade of IPFP across different groups. (A) Differences in PDFF among the normal, mild, and severe IPFP fibrosis groups. (B) Differences in T2* among the normal, mild, and severe IPFP fibrosis groups. (C) Differences in the hypointense signal grade of IPFP among the normal, mild, and severe IPFP fibrosis groups. (**, P<0.01; ****, P<0.0001; ns, no statistical significance). PDFF, proton density fat fraction; IPFP, infrapatellar fat pad.

Table 3 Differences in PDFF, T2*, and hypointense signal grades of IPFP among the normal, mild, and severe IPFP fibrosis groups

Characteristic	Normal (n=23)	Mild fibrosis (n=17)	Severe fibrosis (n=7)	P1	P2	P3
PDFF (%)	77.04±4.05	67.90±4.64	51.08±4.32	<0.0001	<0.0001	<0.0001
T2* (ms)	45.73±9.00	40.49±7.54	23.94±4.22	0.1118	<0.0001	<0.0001
Hypointense signals grade of IPFP	2.22±0.90	2.71±0.92	3.71±0.95	0.3929	0.0037	0.1277

Data are presented as mean ± standard deviation, calculated using one-way ANOVA or Kruskal-Wallis *H* test. P1 = normal *vs.* mild fibrosis patients; P2 = normal *vs.* severe fibrosis patients; P3 = mild fibrosis *vs.* severe fibrosis patients. PDFF, proton density fat fraction; IPFP, infrapatellar fat pad; ANOVA, analysis of variance.

lowest PDFF value. The ANOVA or Kruskal-Wallis *H* test and post hoc analysis also confirmed that there were statistically significant differences between each pair of the groups in terms of PDFF values. The T2* values of IPFP in the normal and mild fibrosis groups were higher than those in the severe fibrosis group, whereas the hypointense signal grade of IPFP was lower in the normal and mild fibrosis groups than in the severe fibrosis group. Both T2* and hypointense signal grades had statistically significant differences between the normal and severe groups and T2* had statistically significant differences between mild and severe groups.

Correlation between PDFF, T2, and hypointense signal grade of IPFP with IPFP fibrosis*

The Spearman correlation results are presented in *Table 4* and *Figure 4*. The PDFF and T2* measurements were significantly and negatively correlated with fibrosis percentage, respectively (ρ=–0.7083 for PDFF, ρ=–0.6028 for T2*, P<0.0001). The hypointense signal grade of the IPFP was positively correlated with fibrosis percentage (ρ=0.4689, P<0.001).

Table 4 The correlation between PDFF and T2*, hypointense signals grade of IPFP and the fibrosis of IPFP

Characteristic	Spearman's Rho (95% CI)	P values
PDFF (%)	–0.7083 (–0.8300 to –0.5224)	<0.0001
T2* (ms)	–0.6028 (–0.7623 to –0.3742)	<0.0001
Hypointense signals grade of IPFP	0.4689 (0.2016 to 0.6712)	0.0009

PDFF, proton density fat fraction; IPFP, infrapatellar fat pad; CI, confidence interval.

Performance of PDFF, T2, hypointense signal grade of IPFP and the combination of PDFF and T2* measurements in diagnosing IPFP fibrosis*

ROC curves were used to evaluate the diagnostic performance of PDFF, T2*, the combination of PDFF and T2*, and the hypointense signal grade of IPFP for diagnosing IPFP fibrosis, distinguishing between non-fibrosis (normal IPFP fibrosis score) and fibrosis (mild, severe, or very severe IPFP fibrosis score) patients (*Figure 5*). Using T2* alone showed an AUC of 0.8098 (95% CI: 0.6878–0.9317), whereas using the hypointense signal grade of IPFP alone had an AUC of 0.7092 (95% CI: 0.5619–0.8566). Using the combination of PDFF and T2* yielded an AUC of 0.9601 (95% CI: 0.9111–1.000), similar to the result of PDFF alone. Using PDFF alone showed an AUC of 0.9529 (95% CI: 0.8937–1.000), its ROC was significantly different from that of T2* (P=0.02266) and hypointense signal grade of IPFP (P=0.00049). However, there were no significant differences in the ROC between using PDFF and T2* and using PDFF alone (P=0.56644) (Table S1).

The optimal cutoff value of PDFF, defined as the point closest to the point (0, 1) on the ROC curve, was 72.15%. With this cut-off, the sensitivity was 87.50% (95% CI: 69.00–95.66%), and the specificity was 91.30% (95% CI: 73.20–98.45%).

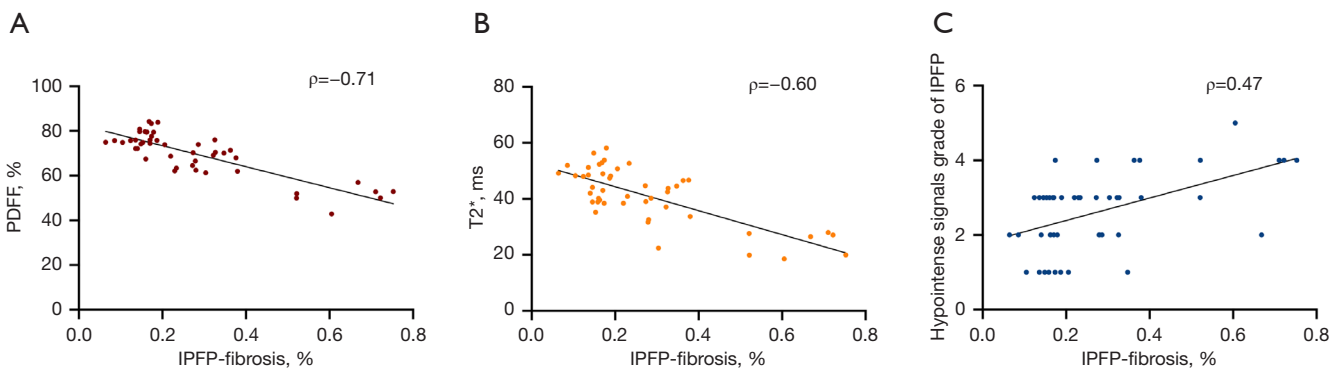

Figure 4 Correlation between different MR values of the IPFP and IPFP fibrosis. (A) Correlation between PDFF of the IPFP and IPFP fibrosis. (B) Correlation between T2* of the IPFP and IPFP fibrosis. (C) Correlation between the hypointense signal grade of the IPFP and IPFP fibrosis. PDFF, proton density fat fraction; IPFP, infrapatellar fat pad; MR, magnetic resonance.

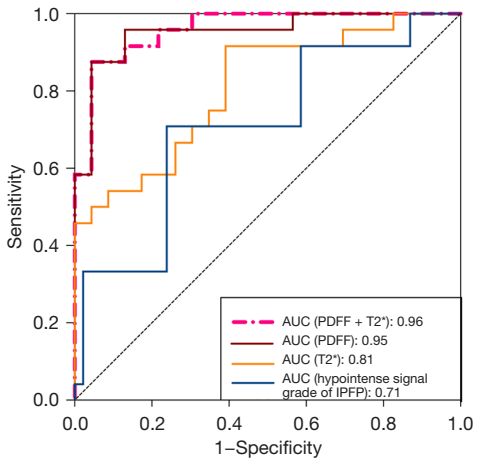

Figure 5 ROC curves for PDFF, T2*, hypointense signal grade of IPFP, and the combination of PDFF and T2* in evaluating the performance of diagnosing IPFP fibrosis. AUC, area under the curve; PDFF, proton density fat fraction; ROC, receiver operating characteristic; IPFP, infrapatellar fat pad.

Linear regression with leave-one-out cross validation showed that with age and sex information, the combination of PDFF and T2* had the best adjusted R^2 of 0.6995. PDFF and T2* models had slightly lower adjusted R^2 of 0.6682 and 0.538 respectively. Linear regression with hypointense signal grade only had an R^2 of 0.1437.

Discussion

This study explored the correlation between PDFF and T2* obtained from MRI and histological IPFP fibrosis measurements. In addition, we examined the potential of using PDFF and T2* as non-invasive measurements to diagnose IPFP fibrosis. As a comparison, we also assessed the hypointense signal grade which is a semi-quantitative measurement associated with fibrosis and other knee symptoms, ensuring consistency with existing methodologies, providing clinically relevant fibrosis indicators, and reducing bias through visual patterns and relative comparisons. This study showed significant differences between each group of different fibrosis scores. T2* in IPFP with severe fibrosis was significantly reduced compared with normal IPFP and mild fibrosis IPFP. PDFF and T2* were significantly negatively correlated with the degree of IPFP fibrosis. PDFF and T2* calculated based on mDixon showed good performance in diagnosing IPFP fibrosis and outperformed the semi-quantitative hypointense signal grade of IPFP, especially PDFF. These results suggest that MRI-derived PDFF is a promising functional imaging tool for monitoring changes in IPFP fibrosis and reflecting the progression of KOA.

mDixon is a water-fat separation sequence based on a chemical shift with six echoes. This sequence has a fast-imaging speed, good spatial coverage, and provides reliable quantitative results due to its precise fat peak modeling and built-in T2* correlation, allowing multiple measurements, such as PDFF and T2*, to be calculated using a single scan. This technique is widely used to predict vertebral osteoporosis (30,31), evaluate benign and malignant bone diseases of the vertebrae (32), detect changes in renal fat and oxygen content in diabetic nephropathy, assess the extent of renal injury in chronic kidney disease (33,34), and evaluate breast density (35,36).

Previous research (21) showed that changes in PDFF and T2* calculated using mDixon technology in the IPFP are associated with knee structural abnormalities and clinical symptoms in the elderly, suggesting that these imaging biomarkers may be reliable tools for assessing KOA progression, with PDFF being particularly noteworthy. In the results of our current pathology-controlled study, PDFF (51.08%±4.32%) and T2* (23.94±4.22 ms) in fibrotic IPFP were significantly reduced compared to mild and normal fibrosis. Our result histologically confirms the ability of PDFF and T2* to assess KOA-related changes. The PDFF and T2* values in this study were lower than those in previous studies, possibly because previous studies were evaluated based on the KOA grouping instead of directly measuring the IPFP fibrosis condition.

PDFF and T2* can distinguish normal, mild, and severe IPFP fibrosis and are significantly negatively correlated with IPFP fibrosis (PDFF: ρ=−0.7083, T2*: ρ=−0.6028). Histologically, increased IPFP fibrosis is usually accompanied by increased vascularization, increased lymphocyte infiltration in the lobular septa, and smaller fat lobules (36), resulting in decreased fat fraction in the adipose tissue (37), and reduced PDFF. A study by Maus *et al.* (38) showed that the R2* signal in the renal cortex of mice was negatively correlated with Masson staining (which assesses fibrosis), consistent with our findings. Fibrous macromolecular tissue reduces T2*, and iron deposition in fibrotic tissue also reduces T2* (39-42). Both revealed the ability of PDFF and T2* to assess tissue fibrosis from the perspectives of tissue structure and molecular changes.

Earlier experimental work in rat KOA models provides crucial translational insight into the MRI changes

observed in clinical situations. Accart *et al.* demonstrated that repeated injections of monosodium urate crystals and lipopolysaccharides into the rat knee joint led to increased synovial fluid volume and IPFP fibrosis, with reduced T2 values correlating histologically with fat loss and extracellular matrix remodeling (43). Similarly, Wang *et al.* revealed that in a rat model of anterior cruciate ligament transection, the T2* relaxation time of the IPFP increased alongside adipocyte degeneration and fibrosis progression, with these changes attributed to edema during inflammation (44). These findings demonstrate MRI changes associated with pathological changes such as fibrosis and fat degeneration in the IPFP, further supporting the clinical relevance of the changes described in our study.

When using the optimal cutoff value of PDFF, the sensitivity was outstanding at 87.50%, with a specificity of 91.30%. This high sensitivity indicates that the technique is highly effective at correctly identifying true positive cases of IPFP fibrosis, making it reliable for early detection. The decent specificity further supports its capability in correctly identifying true negative cases, though there is room for improvement. The balance between sensitivity and specificity suggests that the proposed technique is a robust screening tool, offering a non-invasive, quantitative method for assessing IPFP fibrosis. This makes it particularly valuable in clinical settings where early and accurate diagnosis is crucial for effective patient management and intervention. Moreover, the ability to use PDFF as a reliable biomarker could enhance the overall diagnostic workflow, potentially reducing the need for more invasive procedures such as biopsies and improving patient outcomes through earlier and more precise treatment planning.

In the study by Torriani *et al.*, shortened T2 relaxation values of the IPFP were observed post-arthroscopic knee surgery, suggesting fat tissue fibrosis (45). Similarly, multi-acquisition variable-resonance image combination (MAVRIC)-based T2 mapping revealed IPFP scar formation after total knee arthroplasty, with T2 value reduction correlating with scar severity (46). Traditional imaging methods for assessing fibrosis, such as T2-weighted imaging signal scoring, provide stable image quality and effectively distinguish differences in tissue water content. However, these methods rely on subjective observer judgment, are prone to inter-observer variability, and are insensitive to subtle magnetic field changes, which limit their applicability. In contrast, T2* is highly sensitive to magnetic susceptibility changes, enabling assessment of fibrosis-related tissue composition alterations related to iron deposition or abnormal blood distribution during fibrosis. T2* allows quantitative post-processing, reflects microenvironmental susceptibility, and offers faster imaging. As demonstrated in this study, the inter-observer reproducibility and correlation of the hypointense signal grade of IPFP with IPFP fibrosis were lower than those of PDFF and T2*, and PDFF and T2* also outperformed the hypointense signal grade of IPFP in distinguishing normal and fibrotic conditions.

Limitations

First, the sample size of the study was relatively small, and the number of patients in the severe fibrosis group was limited, necessitating larger and more comprehensive patient samples, as well as multicenter and longitudinal studies. Second, pathological changes in fibrotic IPFP may include inflammation, edema, and iron deposition. The current staining is primarily focused on assessing fibrosis and it cannot visualize edema and inflammation effectively. Future studies should explore the relationship between MR measurement parameters and specific pathological changes in detail to comprehensively evaluate their clinical significance. Third, there is a certain discrepancy between the morphological features and spatial correspondence of preoperative MR imaging and postoperative tissue sections. Lastly, IPFP segmentation was performed manually in this study. Automated or semi-automated segmentation can be more efficient and further improve the accuracy of the quantitative measurements. In future studies, we will compare manual segmentation with automated or semi-automated segmentation to quantify IPFP MRI parameters and determine the optimal method.

Conclusions

This prospective pathology-controlled study demonstrated the feasibility of using PDFF and T2* based on mDixon calculations as non-invasive imaging biomarkers for the quantitative diagnosis and assessment of IPFP fibrosis. PDFF and T2* were significantly correlated with the degree of IPFP fibrosis. This may help clinicians to objectively diagnose and assess IPFP fibrosis and promote the development of individualized treatments for KOA.

Acknowledgments

The authors express deep gratitude to the Innovation

Platform of Regeneration and Repair of Spinal Cord and Nerve Injury, Department of Orthopedic Surgery, The Seventh Affiliated Hospital, Sun Yat-sen University for their invaluable support for this research.

Footnote

Reporting Checklist: The authors have completed the STARD reporting checklist. Available at https://qims.amegroups.com/article/view/10.21037/qims-24-2021/rc

Funding: This work was in part supported by National Natural Science Foundation of China (grant No. 82471928) and the Guangdong Basic and Applied Basic Research Foundation (grant Nos. 2024A1515010352 and 2022A1515012545). These two fundings are to authors B.Z., J.W., Q.Y., K.J., Xinru Zhang, Y.C., and Xiaodong Zhang; the other authors received no financial support from any source other than their affiliated institutes for the research, authorship, and publication of this work.

Conflicts of Interest: All authors have completed the ICMJE uniform disclosure form (available at https://qims.amegroups.com/article/view/10.21037/qims-24-2021/coif). The authors have no conflicts of interest to declare.

Ethical Statement: The authors are accountable for all aspects of the work in ensuring that questions related to the accuracy or integrity of any part of the work are appropriately investigated and resolved. The study was conducted in accordance with the Declaration of Helsinki (as revised in 2013). The study protocol was approved by the Ethics Committee of The Third Affiliated Hospital, Southern Medical University (No. 2024-lunshen-008) and informed consent was provided by all individual participants.

References

1. Sharma L. Osteoarthritis of the Knee. N Engl J Med 2021;384:51-9.
2. Cui A, Li H, Wang D, Zhong J, Chen Y, Lu H. Global, regional prevalence, incidence and risk factors of knee osteoarthritis in population-based studies. EClinicalMedicine 2020;29-30:100587.
3. Wang Z, Lu J, Li Z, Wang Y, Ge H, Zhang M, Wang R, Gu Y, Ding L, Ren W, Shen Z, Du G, Wu Y, Zhan H. Qualitative and Quantitative Measures in the Infrapatellar Fat Pad in Older Adults: Associations with Knee Pain, Radiographic Osteoarthritis, Kinematics, and Kinetics of the Knee. Acad Radiol 2024;31:3315-26.
4. Tang S, Yao L, Ruan J, Kang J, Cao Y, Nie X, Lan W, Zhu Z, Han W, Liu Y, Tian J, Seale P, Qin L, Ding C. Single-cell atlas of human infrapatellar fat pad and synovium implicates APOE signaling in osteoarthritis pathology. Sci Transl Med 2024;16:eadf4590.
5. Stocco E, Belluzzi E, Contran M, Boscolo-Berto R, Picardi E, Guidolin D, Fontanella CG, Olivotto E, Filardo G, Borile G, Romanato F, Ramonda R, Ruggieri P, Favero M, Porzionato A, De Caro R, Macchi V. Age-Dependent Remodeling in Infrapatellar Fat Pad Adipocytes and Extracellular Matrix: A Comparative Study. Front Med (Lausanne) 2021;8:661403.
6. Barboza E, Hudson J, Chang WP, Kovats S, Towner RA, Silasi-Mansat R, Lupu F, Kent C, Griffin TM. Profibrotic Infrapatellar Fat Pad Remodeling Without M1 Macrophage Polarization Precedes Knee Osteoarthritis in Mice With Diet-Induced Obesity. Arthritis Rheumatol 2017;69:1221-32.
7. Favero M, El-Hadi H, Belluzzi E, Granzotto M, Porzionato A, Sarasin G, Rambaldo A, Iacobellis C, Cigolotti A, Fontanella CG, Natali A, Ramonda R, Ruggieri P, De Caro R, Vettor R, Rossato M, Macchi V. Infrapatellar fat pad features in osteoarthritis: a histopathological and molecular study. Rheumatology (Oxford) 2017;56:1784-93.
8. Fontanella CG, Belluzzi E, Pozzuoli A, Favero M, Ruggieri P, Macchi V, Carniel EL. Mechanical behavior of infrapatellar fat pad of patients affected by osteoarthritis. J Biomech 2022;131:110931.
9. Li J, Gui T, Yao L, Guo H, Lin YL, Lu J, Duffy M, Zgonis M, Mauck R, Dyment N, Zhang Y, Scanzello C, Seale P, Qin L. Synovium and infrapatellar fat pad share common mesenchymal progenitors and undergo coordinated changes in osteoarthritis. J Bone Miner Res

2024;39:161-76.
10. Han W, Aitken D, Zhu Z, Halliday A, Wang X, Antony B, Cicuttini F, Jones G, Ding C. Hypointense signals in the infrapatellar fat pad assessed by magnetic resonance imaging are associated with knee symptoms and structure in older adults: a cohort study. Arthritis Res Ther 2016;18:234.
11. Yue S, Zhai G, Zhao S, Liang X, Liu Y, Zheng J, Chen X, Dong Y. The biphasic role of the infrapatellar fat pad in osteoarthritis. Biomed Pharmacother 2024;179:117364.
12. An JS, Tsuji K, Onuma H, Araya N, Isono M, Hoshino T, Inomata K, Hino J, Miyazato M, Hosoda H, Kangawa K, Nakagawa Y, Katagiri H, Miyatake K, Sekiya I, Muneta T, Koga H. Inhibition of fibrotic changes in infrapatellar fat pad alleviates persistent pain and articular cartilage degeneration in monoiodoacetic acid-induced rat arthritis model. Osteoarthritis Cartilage 2021;29:380-8.
13. Grevenstein D, Heilig J, Dargel J, Oppermann J, Eysel P, Brochhausen C, Niehoff A. COMP in the Infrapatellar Fat Pad-Results of a Prospective Histological, Immunohistological, and Biochemical Case-Control Study. J Orthop Res 2020;38:747-58.
14. Luo P, Lu L, Xu R, Jiang L, Li G. Gaining Insight into Updated MR Imaging for Quantitative Assessment of Cartilage Injury in Knee Osteoarthritis. Curr Rheumatol Rep 2024;26:311-20.
15. Li J, Fu S, Gong Z, Zhu Z, Zeng D, Cao P, Lin T, Chen T, Wang X, Lartey R, Kwoh CK, Guermazi A, Roemer FW, Hunter DJ, Ma J, Ding C. MRI-based Texture Analysis of Infrapatellar Fat Pad to Predict Knee Osteoarthritis Incidence. Radiology 2022;304:611-21.
16. Perry TA, Yang X, van Santen J, Arden NK, Kluzek S. Quantitative and semi-quantitative assessment of synovitis on MRI and the relationship with symptoms in symptomatic knee osteoarthritis. Rheumatology (Oxford) 2021;60:1763-73.
17. Tan H, Kang W, Fan Q, Wang B, Yu Y, Yu N, Duan H, Yuan P, Wang S, Chen Q, Jin C. Intravoxel Incoherent Motion Diffusion-Weighted MR Imaging Findings of Infrapatellar Fat Pad Signal Abnormalities: Comparison Between Symptomatic and Asymptomatic Knee Osteoarthritis. Acad Radiol 2023;30:1374-83.
18. Fontanella CG, Belluzzi E, Pozzuoli A, Scioni M, Olivotto E, Reale D, Ruggieri P, De Caro R, Ramonda R, Carniel EL, Favero M, Macchi V. Exploring Anatomo-Morphometric Characteristics of Infrapatellar, Suprapatellar Fat Pad, and Knee Ligaments in Osteoarthritis Compared to Post-Traumatic Lesions. Biomedicines 2022;10:1369.
19. Cen H, Yan Q, Han W, Meng T, Chen Z, Ruan G, Wang T, Pan F, Chen D, Kraus VB, Hunter DJ, Ding C. Longitudinal association of infrapatellar fat pad signal intensity alteration with biochemical biomarkers in knee osteoarthritis. Rheumatology (Oxford) 2022;62:439-49.
20. Cao MJ, Wu WJ, Chen JW, Fang XM, Ren Y, Zhu XW, Cheng HY, Tang QF. Quantification of ectopic fat storage in the liver and pancreas using six-point Dixon MRI and its association with insulin sensitivity and β-cell function in patients with central obesity. Eur Radiol 2023;33:9213-22.
21. Chen Y, Zhang X, Li M, Zhong L, Ding Y, Zhang Y, Du X, Mo X, Chen J, Chen Q, Huang W, Zhong S, Zhang X. Quantitative MR evaluation of the infrapatellar fat pad for knee osteoarthritis: using proton density fat fraction and T2* relaxation based on DIXON. Eur Radiol 2022;32:4718-27.
22. Altman RD, Gold GE. Atlas of individual radiographic features in osteoarthritis, revised. Osteoarthritis Cartilage 2007;15 Suppl A:A1-56.
23. The Joint Surgery Branch of the Chinese Orthopaedic Association, The Subspecialty Group of Osteoarthritis, Chinese Association of Orthopaedic Surgeons, The National Clinical Research Center for Geriatric Disorders (Xiangya Hospital), Editorial Office of Chinese Journal of Orthopaedics. Guidelines for the Diagnosis and Treatment of Osteoarthritis in China (2021 Edition). Chinese Journal of Orthopedics 2021;41:1291-314.
24. Wang J, Zhang H, Chen L, Fu K, Yan Y, Liu Z. CircDCBLD2 alleviates liver fibrosis by regulating ferroptosis via facilitating STUB1-mediated PARK7 ubiquitination degradation. J Gastroenterol 2024;59:229-49.
25. Seyed-Razavi Y, Lee SR, Fan J, Shen W, Cornish EE, Gillies MC. JR5558 mice are a reliable model to investigate subretinal fibrosis. Sci Rep 2024;14:18752.
26. Onuma H, Tsuji K, Hoshino T, Inomata K, Udo M, Nakagawa Y, Katagiri H, Miyatake K, Watanabe T, Sekiya I, Muneta T, Koga H. Fibrotic changes in the infrapatellar fat pad induce new vessel formation and sensory nerve fiber endings that associate prolonged pain. J Orthop Res 2020;38:1296-306.
27. Krkoska P, Kokosova V, Dostal M, Vlazna D, Kerkovsky M, Straka M, Gerstberger R, Matulova K, Ovesna P, Adamova B. Assessment of lumbar paraspinal muscle morphology using mDixon Quant magnetic resonance imaging (MRI):

a cross-sectional study in healthy subjects. Quant Imaging Med Surg 2024;14:6015-35.
28. Bainbridge A, Bray TJP, Sengupta R, Hall-Craggs MA. Practical Approaches to Bone Marrow Fat Fraction Quantification Across Magnetic Resonance Imaging Platforms. J Magn Reson Imaging 2020;52:298-306.
29. Nakagawa Y, Tsuji K, Nakamura T, Katagiri H, Ozeki N, Shioda M, An JS, Yoshida R, Sekiya I, Koga H. Association of Infrapatellar Fat Pad Fibrosis at 3 Months After ACL Reconstruction With Short-term Clinical Outcomes and Inflammatory Cytokine Levels in the Synovial Fluid. Orthop J Sports Med 2023;11:23259671231164122.
30. Zhao Y, Zhao T, Chen S, Zhang X, Serrano Sosa M, Liu J, Mo X, Chen X, Huang M, Li S, Zhang X, Huang C. Fully automated radiomic screening pipeline for osteoporosis and abnormal bone density with a deep learning-based segmentation using a short lumbar mDixon sequence. Quant Imaging Med Surg 2022;12:1198-213.
31. Zhao Y, Huang M, Ding J, Zhang X, Spuhler K, Hu S, Li M, Fan W, Chen L, Zhang X, Li S, Zhou Q, Huang C. Prediction of Abnormal Bone Density and Osteoporosis From Lumbar Spine MR Using Modified Dixon Quant in 257 Subjects With Quantitative Computed Tomography as Reference. J Magn Reson Imaging 2019;49:390-9.
32. Bacher S, Hajdu SD, Maeder Y, Dunet V, Hilbert T, Omoumi P. Differentiation between benign and malignant vertebral compression fractures using qualitative and quantitative analysis of a single fast spin echo T2-weighted Dixon sequence. Eur Radiol 2021;31:9418-27.
33. Wang Y, Ju Y, An Q, Lin L, Liu AL. mDIXON-Quant for differentiation of renal damage degree in patients with chronic kidney disease. Front Endocrinol (Lausanne) 2023;14:1187042.
34. Yang C, Wang Z, Zhang J, Wang Y, Wang Z, Wang H, Wang Y, Li W. MRI Assessment of Renal Lipid Deposition and Abnormal Oxygen Metabolism of Type 2 diabetes Mellitus Based on mDixon-Quant. J Magn Reson Imaging 2023;58:1408-17.
35. Ding J, Stopeck AT, Gao Y, Marron MT, Wertheim BC, Altbach MI, Galons JP, Roe DJ, Wang F, Maskarinec G, Thomson CA, Thompson PA, Huang C. Reproducible automated breast density measure with no ionizing radiation using fat-water decomposition MRI. J Magn Reson Imaging 2018;48:971-81.
36. Ying J, Cattell R, Zhao T, Lei L, Jiang Z, Hussain SM, Gao Y, Chow HS, Stopeck AT, Thompson PA, Huang C. Two fully automated data-driven 3D whole-breast segmentation strategies in MRI for MR-based breast density using image registration and U-Net with a focus on reproducibility. Vis Comput Ind Biomed Art 2022;5:25.
37. Li J, Lu X, Zhu Z, Kalutkiewicz KJ, Mounajjed T, Therneau TM, Venkatesh SK, Sui Y, Glaser KJ, Hoodeshenas S, Manduca A, Shah VH, Ehman RL, Allen AM, Yin M. Head-to-head comparison of magnetic resonance elastography-based liver stiffness, fat fraction, and T1 relaxation time in identifying at-risk NASH. Hepatology 2023;78:1200-8.
38. Maus M, López-Polo V, Mateo L, Lafarga M, Aguilera M, De Lama E, et al. Iron accumulation drives fibrosis, senescence and the senescence-associated secretory phenotype. Nat Metab 2023;5:2111-30.
39. Li J, Wang Y, Zhang X, Zhang P, Su Y, Bai L, Wang Y, Wang M, Zhao J. Associations of muscle size and fatty infiltration with bone mineral density of the proximal femur bone. Front Endocrinol (Lausanne) 2022;13:990487.
40. Chen Y, Ren D, Guan X, Yang HJ, Liu T, Tang R, Ho H, Jin H, Zeng M, Dharmakumar R. Quantification of myocardial hemorrhage using T2* cardiovascular magnetic resonance at 1.5T with ex-vivo validation. J Cardiovasc Magn Reson 2021;23:104.
41. Topiwala A, Wang C, Ebmeier KP, Burgess S, Bell S, Levey DF, Zhou H, McCracken C, Roca-Fernández A, Petersen SE, Raman B, Husain M, Gelernter J, Miller KL, Smith SM, Nichols TE. Associations between moderate alcohol consumption, brain iron, and cognition in UK Biobank participants: Observational and mendelian randomization analyses. PLoS Med 2022;19:e1004039.
42. Meloni A, De Marchi D, Pistoia L, Grassedonio E, Peritore G, Preziosi P, Restaino G, Righi R, Riva A, Renne S, Schicchi N, Vallone A, Peluso A, Gerardi C, Positano V, Pepe A. Multicenter validation of the magnetic resonance T2* technique for quantification of pancreatic iron. Eur Radiol 2019;29:2246-52.
43. Accart N, Dawson J, Obrecht M, Lambert C, Flueckiger M, Kreider J, Hatakeyama S, Richards PJ, Beckmann N. Degenerative joint disease induced by repeated intra-articular injections of monosodium urate crystals in rats as investigated by translational imaging. Sci Rep 2022;12:157.
44. Wang CY, Tsai PH, Siow TY, Lee HS, Chang YC, Hsu YC, Chiang SW, Lin MH, Chung HW, Huang GS. Change in T2* relaxation time of Hoffa fat pad correlates with histologic change in a rat anterior cruciate ligament transection model. J Orthop Res 2015;33:1348-55.
45. Torriani M, Taneja AK, Hosseini A, Gill TJ, Bredella MA,

Li G. T2 relaxometry of the infrapatellar fat pad after arthroscopic surgery. Skeletal Radiol 2014;43:315-21.
46. Sacher SE, Neri JP, Gao MA, Argentieri EC, Potter HG, Koch KM, Koff MF. MAVRIC based T2 mapping assessment of infrapatellar fat pad scarring in patients with total knee arthroplasty. J Orthop Res 2023;41:1299-309.

Cite this article as: Zhou B, Wu J, Zhao T, Yu Q, Jiang K, Zhang X, Wei Q, Zhang R, Fang H, Zhang H, Chen Y, Zhang X, Huang C. Quantification of infrapatellar fat pad fibrosis using magnetic resonance imaging-derived proton density fat fraction: a pathology-controlled study. Quant Imaging Med Surg 2025;15(4):2694-2706. doi: 10.21037/qims-24-2021